Machine learning enabled velocity model building with uncertainty quantification

Rafael Orozco^a, Huseyin Tuna Erdinc^a, Yunlin Zeng^a, Mathias Louboutin^b, Felix J. Herrmann^a

^a Georgia Institute of Technology, ^b Devito Codes,

Abstract

Accurately characterizing migration velocity models is crucial for a wide range of geophysical applications, from hydrocarbon exploration to monitoring of CO₂ sequestration projects. Traditional velocity model building methods such as Full-Waveform Inversion (FWI) are powerful but often struggle with the inherent complexities of the inverse problem, including noise, limited bandwidth, receiver aperture and computational constraints. To address these challenges, we propose a scalable methodology that integrates generative modeling, in the form of Diffusion networks, with physics-informed summary statistics, making it suitable for complicated imaging problems including field datasets. By defining these summary statistics in terms of subsurface-offset image volumes for poor initial velocity models, our approach allows for computationally efficient generation of Bayesian posterior samples for migration velocity models that offer a useful assessment of uncertainty. To validate our approach, we introduce a battery of tests that measure the quality of the inferred velocity models, as well as the quality of the inferred uncertainties. With modern synthetic datasets, we reconfirm gains from using subsurface-image gathers as the conditioning observable. For complex velocity model building involving salt, we propose a new iterative workflow that refines amortized posterior approximations with salt flooding and demonstrate how the uncertainty in the velocity model can be propagated to the final product reverse time migrated images. Finally, we present a proof of concept on field datasets to show that our method can scale to industry-sized problems.

1. Introduction

Subsurface characterization of the earth's subsurface is important for hydrocarbon exploration (Zhang et al., 2022), monitoring of CO₂ storage projects

Email address: rorozco@gatech.edu (Rafael Orozco)

^{*}Corresponding author

(Gahlot et al., 2024), geothermal energy projects (Louie et al., 2012) and various other applications (Wagner and Uhlemann, 2021). Generally, subsurface characterization is achieved by observing the interaction between specific physical phenomena (such as electrodynamics, gravity, and acoustic wave propagation) and subsurface properties. This tomographic information is then resolved into images that are analyzed for different characterization requirements. Although our framework is generally applicable, we focus on characterization of acoustic properties by means of probing the subsurface with acoustic waves. Out of the various methods, FWI stands out as a powerful tool due to its ability to resolve high-quality acoustic images in complex structures (Tarantola, 1984). In spite of its advantages, FWI still has shortcomings due in part to the nature of the problem but also due to the specific computational challenges that FWI brings since it requires solving many wave-equation partial differential equations (PDEs).

The particular challenges of the FWI inverse problem are that the observations are corrupted by noise, are limited in frequency bandwidth, computational simulations will always contain some approximation to the true physics and due to practical engineering considerations are mostly restricted to sensing the upcoming waves at the surface so will suffer from some sort of limited aperture. All of these factors contribute to FWI's ill-posed nature in the sense that many subsurface scenarios are capable of explaining the limited data available. Traditional workflows approach this challenge by introducing prior information to regularize the vast search space, such as Total Variation (TV) (Esser et al., 2018). While this has served well to produce deterministic solutions, it does not express the multi-solution nature of FWI and does not represent a realistic prior of the multiscale complexity of Earth structures.

We use Bayesian inference as a principled framework to combine observable data (seismic shot gathers) with prior knowledge (training samples) and output a family of Earth models that give users practical uncertainty quantification (UQ). One of the major gaps in geophysical inversion is the difficulty of computing Bayesian posterior distributions that are grounded in useful prior information and incorporate the complex physics of the problem. Existing approaches either are too expensive to scale to large-scale problems (sampling-based methods), fail to capture the full extent of uncertainty (local methods), or rely on approximations that weaken the physical fidelity of the results (convolution-based methods).

As a form of variational inference (Jordan et al., 1999), our approach sidesteps the computational problem of sampling the posterior distribution by optimizing instead for an amortized (read generalized) approximation to the posterior that is learned from training examples and can be applied computationally efficiently at test time with small compute (as measured by PDE solves) on various datasets.

2. Paper outline

First, we introduce the wave-based inversion problem that we aim to solve. Due to the ill-posed nature of the problem, we use a Bayesian formulation to solve it. Then, we discuss related work that has solved various aspects of this problem, highlighting the gap in this literature that we aim to fill. We explain our particular methods, which include simulation-based inference (SBI) and conditional Diffusion networks as the core generative network. We then explain the use of physical summary statistics to efficiently incorporate the wave physics into the method. To evaluate the quality of our posterior distributions, we propose four distinct metrics, each targeting a different aspect of UQ. These metrics are applied to assess the improvements gained from using Common-Image Gathers (CIGs) in comparison to Reverse-Time Migrations (RTMs, which are CIGs at zero subsurface offset). Next, we address the challenges presented by the complex salt structures in the SEAM model (Fehler and Keliher, 2011). To overcome these, we recognize the need for additional guidance from the physics and propose an iterative algorithm, ASPIRE, that leverages the wave PDE while minimizing the total number of PDEs at inference time. Finally, we test the robustness and scalability of our method by applying it to field datasets. The results demonstrate that the method is adaptable to changes in the test distribution and can handle large-scale 2D inversion problems (e.g., 512×7024 grid sizes).

3. Problem statement

The core of subsurface characterization involves solving an inverse problem where the objective is to infer unknown subsurface properties from observational data. In this context, the forward process, represented as

$$\mathbf{v} = \mathcal{F}(\mathbf{x}) + \boldsymbol{\varepsilon},\tag{1}$$

describes how the observations (shot records) \mathbf{y} are generated from the underlying subsurface properties \mathbf{x} , with $\boldsymbol{\varepsilon}$ representing bandwidth-limited noise. Here, we focus on wave-based inversion, where the forward operator \mathcal{F} corresponds to the solution of the wave-equation PDE with the wavefield being restricted to the positions of the receivers. The complexity of this problem arises from the null-space present in the forward operator, compounded by noise in the measurements, which makes direct inversion unreliable as it fails to characterize the full solution.

To model the noise in the system, one would assume that the noise ε follows a known distribution, such as a normal distribution $N(0,\sigma)$. This leads to a likelihood function $p(\mathbf{y} \mid \mathbf{x})$, which quantifies the probability of observing the data \mathbf{y} given the unknown parameters \mathbf{x} . If the noise is additive, the likelihood can be written as a well-known ℓ_2 -normed misfit, $p(\mathbf{y}|\mathbf{x}) = \frac{1}{2\sigma^2} ||\mathcal{F}(\mathbf{x}) - \mathbf{y}||_2^2$. Minimizing data misfits of this form underpins FWI and other variational methods that use the forward model's fit to the data, but on their own, it is insufficient to

fully resolve the inverse problem due to the non-uniqueness of solutions and the presence of possibly adverse parasitic local minima.

In this paper, we address this limitation by adopting a Bayesian approach to the inverse problem. Our target in this paper is that given an observation from the field \mathbf{y} we aim to find samples from the posterior distribution $\mathbf{x}_{\text{post}} \sim p(\mathbf{x}|\mathbf{y})$, which can be defined using Bayes's rule as the combination of the prior and the data likelihood $p(\mathbf{x} \mid \mathbf{y}) \propto p(\mathbf{y} \mid \mathbf{x})p(\mathbf{x})$. This posterior distribution combines the prior information about the subsurface properties, encoded in $p(\mathbf{x})$, with the likelihood of observing the data, $p(\mathbf{y} \mid \mathbf{x})$, resulting in a probabilistic representation of the subsurface model that accounts for both the uncertainty in the data and the prior knowledge. This Bayesian framework allows for a more robust characterization of subsurface properties, as it provides not just a single estimate but a distribution of plausible solutions, incorporating uncertainty into the interpretation.

4. Related work and our contributions

The literature on solving the FWI problem with uncertainty has primarily focused on implementations of Stein Variational Gradient Descent (SVGD) methods. The foundational work in this area was introduced by (Zhao et al., 2022), who applied Bayesian seismic tomography using normalizing flows. Later, the same authors extended their method to 3D inversion (Zhang et al., 2023), though this approach still required numerous forward and adjoint PDE solutions for each observation, which made it computationally expensive.

In an effort to reduce the computational burden of SVGD methods, (Izzatullah et al., 2024) proposed a technique that minimizes the number of optimization iterations by carefully defining the prior distribution. This approach begins with solving the FWI problem under the assumption of convergence and then adds perturbations to the solution to create a prior distribution. This prior is used as an initial ensemble in an SVGD technique to optimize toward individual maximum likelihood estimates (MLEs) that do not collapse into the same solution due to a repulsion term in the method. Although the authors did not use true prior terms—thus these solutions are not precise Bayesian samplesthey presented samples that revealed interesting variations between them and were mostly focused on the areas of the image with low illumination from the source-receiver configuration. (Yang et al., 2024) extended these concepts by combining ideas from the Deep Image Prior (DPI) with conditional networks. They performed an SVGD-like update starting from an ensemble of models that surrounded a precomputed FWI solution, as in (Izzatullah et al., 2024), to fine-tune the weights of a pretrained conditional network. This pretraining process enabled them to sample various Earth models by post hoc changes to the network conditions. While this takes regularization benefits of both the untrained DPI and the features learned during pretraining, it also does not have a clear prior used during optimization, so does not correspond to true Bayesian samples over the target in this case the uncertainty over network parameters.

In the context of defining realistic Earth priors, (Zhao and Curtis, 2024) assumed constrained Gaussian distributions over the prior, which were fitted to real Earth data. They then implemented a secondary optimization that bypasses the likelihood, making it efficient to swap different priors at inference time. (Qu et al., 2024) explored another important aspect of UQ by employing importance sampling and ensemble methods. Their objective was to capture uncertainty stemming not only from the ill-posed nature of the inverse problem but also from epistemic uncertainty in the network weights.

Similar work using normalizing flows includes (Sun et al., 2024), which targets time-lapse inversion. They formed training samples by performing FWI inversion on prior examples to construct the training dataset. The prior samples assumed access to a non-cycle-skipped starting model, to which various perturbations were added, resulting in a diverse set of training samples. In a related approach, (Sun and Williamson, 2024) utilized invertible networks with a maximum mean discrepancy (MMD)-based loss. Given that MMD estimation requires large batch sizes, the authors applied model and data reduction techniques to minimize memory usage and make the training feasible. Though not specifically aimed at UQ, (Muller et al., 2023) presented a method similar to our iterative refinement, by using an iterative scheme to refine the migration velocity models. Targeting our same application of salt velocity model building, (Alali et al., 2023) combine trained convolutional neural networks with FWI updates to automatically build salt velocity models. Here, we aim to deliver automatic salt model building but without the cost associated with FWI workflows, while also providing uncertainty quantification.

This paper builds on the methods introduced in previous literature of applying variational inference methods towards seismic imaging (Siahkoohi et al., 2023; Orozco et al., 2024) that have the goal of calculating Bayesian samples while making frugal use of the physical operator by defining an expensive offline training phase to achieve a cheap online inference phase. In particular, we build on the WISE framework (Yin et al., 2024b) with the use of conditional Diffusion networks to improve results by leveraging the prior learning capabilities of Diffusion (Ho et al., 2020). While Structural Similarity Index Metric (SSIM) (Brunet et al., 2011) and Root Mean Squared Error (RMSE) can compare the quality between image reconstructions, it remains unclear in the literature how to compare two results for uncertainty. We therefore propose and discuss a battery of metrics that can be used to benchmark the quality of the uncertainty. Furthermore, we discuss a method to improve on amortized results with minimal extra computation at test time and then demonstrate these methods on field data in preliminary proof of concepts.

Our key contributions include:

- 1. Extending the WISE framework to incorporate conditional Diffusion networks.
- 2. Proposing four benchmark metrics to assess the quality of UQ.
- 3. Testing our method on the Compass and Synthoseis training datasets,

demonstrating the value of using Common Image Gathers (CIGs) over Reverse Time Migrations (RTMs) alone from the standpoint of image quality and also uncertainty quality.

- 4. Introducing the iterative ASPIRE algorithm for seismic inversion, particularly for complex salt structures, such as those in the SEAM model.
- 5. Presenting a proof-of-concept application on field datasets to demonstrate the scalability of the method.

5. Methods

Our approach builds on the simulation-based inference (SBI) framework (Cranmer et al., 2020), a powerful tool for solving inverse problems that leverages numerical simulations and conditional generative networks to approximate posterior distributions. While SBI is, in principle, a general method, directly applying it to the complex problem of seismic subsurface characterization presents significant challenges due to the intricacies of waveform data. To address these challenges, we incorporate conditional Diffusion networks as the generative backbone, enabling the learning of an expressive prior and scalable posterior sampling. Additionally, we employ physics-based summary statistics to compress observational data while preserving crucial information about the subsurface properties.

5.1. Simulation-based inference

SBI combines the strengths of numerical simulations and conditional generative modeling, providing a powerful framework for solving complex inverse problems (Cranmer et al., 2020). Numerical simulations are used to generate data pairs, $\mathcal{D} = \{\mathbf{x}^i, \mathbf{y}^i\}_{i=0}^N$, where each pair consists of a set of subsurface properties \mathbf{x}^i and the corresponding simulated observation \mathbf{y}^i derived using the forward simulation Equation 1. These data pairs are then used to train a conditional generative network which learns the posterior distribution of the unknown properties given the observations. By integrating physics-based simulations with modern generative modeling techniques, SBI provides an amortized method—that is, it generalizes over all data simulated from the realizations of the prior. This means that after an initial training phase, inference is inexpensive and can be done on many unseen test observations without retraining or expensive applications of the forward/adjoint operator.

5.2. Conditional generative modeling with Diffusion networks

Diffusion networks are density estimation algorithms based on learning the score of the target distribution $\nabla_{\mathbf{x}} \log p(\mathbf{x})$ (Song et al., 2020). Specifically, we define a family of mollified distributions $\nabla_{\mathbf{x}} \log p(\mathbf{x}, \sigma(t))$, where $\sigma(t)$ represents a noise schedule such that, as time t increases, the distribution is mollified towards the Gaussian distribution. After learning the score for all time steps t, Diffusion networks can evaluate likelihoods (Zheng et al., 2023) and sample new generative instances from the target distribution $p(\mathbf{x})$. To learn the score,

Diffusion networks use one of the many forms of the denoising objective (Karras et al., 2022),

$$\hat{\theta} = \underset{\theta}{\operatorname{argmin}} \ \mathbb{E}_{\mathbf{x} \sim p(\mathbf{x})} \mathbb{E}_{\mathbf{n} \sim \mathcal{N}(0, t^2 I)} \| s_{\theta}(\mathbf{x} + \mathbf{n}; t) - \mathbf{x} \|_2^2$$

where the approximation the score at time t is given by the evaluation of the trained network $s_{\hat{\theta}}(\mathbf{x}, t)$. New samples from the target distribution can be generated by solving the following stochastic differential equation (SDE):

$$d\mathbf{x} = -\dot{\sigma}(t)\sigma(t)\nabla_{\mathbf{x}}p(\mathbf{x};\sigma(t))dt. \tag{2}$$

Here, we use the formulation in Karras et al. (2022) to simplify terms. Many strategies exist for solving this SDE. Here, we follow the method in Karras et al. (2022) and use a procedure similar to the predictor-corrector sampler of Song et al. (2020).

To extend Diffusion networks towards conditional distributions, we aim to find the conditional score $\nabla_{\mathbf{x}} \log p(\mathbf{x}|\mathbf{y})$. Based on the theory laid out in Batzolis et al. (2021) and Baldassari et al. (2024), we can approximate this conditional score with a simple modification of Diffusion networks by incorporating the observation \mathbf{y} as an additional condition to the denoising network

$$\hat{\theta} = \underset{\boldsymbol{\theta}}{\operatorname{argmin}} \ \mathbb{E}_{\mathbf{y} \sim p(\mathbf{y}|\mathbf{x})} \mathbb{E}_{\mathbf{x} \sim p(\mathbf{x})} \mathbb{E}_{\mathbf{n} \sim \mathcal{N}(0, t^2 I)} \| s_{\boldsymbol{\theta}}(\mathbf{x} + \mathbf{n}, \mathbf{y}, t) - \mathbf{x} \|_{2}^{2}.$$

In many cases, implementing a conditional Diffusion network involves simple modifications to existing non-conditional Diffusion networks. In Github Repo, we share our conditional Diffusion implementation derived from non-conditional networks from Elucidating Diffusion Models (Karras et al., 2022). In practice, we approximate the expectation over prior samples with a set of ground truth examples and sample from the likelihood by running the simulator in Equation 1 to form a paired dataset $\mathcal{D} = \{(\mathbf{x}^i, \mathbf{y}^i)_{i=0}^N, \text{ then perform stochastic gradient descent on the following objective:}$

$$\hat{\theta} = \underset{\boldsymbol{\theta}}{\operatorname{argmin}} \ \mathcal{L}(\mathcal{D}, \boldsymbol{\theta}) = \underset{\boldsymbol{\theta}}{\operatorname{argmin}} \ \sum_{i=0}^{N} \mathbb{E}_{\mathbf{n} \sim \mathcal{N}(0, t^{2}I)} \| s_{\boldsymbol{\theta}}(\mathbf{x}^{i} + \mathbf{n}, \mathbf{y}^{i}, t) - \mathbf{x}^{i} \|_{2}^{2}.$$
(3)

After training, conditional Diffusion generates samples from the posterior $p(\mathbf{x} \mid \mathbf{y}^{\text{obs}})$ by conditioning the network on \mathbf{y}^{obs} and following the reverse process on the same SDE as in Equation 2 to generate a posterior sample \mathbf{x}_{post} . While the physics of the inverse problem is present in the formation of the dataset, this is insufficient in the case of complex forward operators associated with the wave equation (Orozco et al., 2023). Therefore, we will explore a method to alleviate this challenge next by incorporating more physics into the methodology.

5.3. Physics-based summary statistics

While simulation-based inference (SBI) has shown promise across various fields, applying it to problems with complex forward operators, such as seismic inversion, presents unique challenges. These challenges stem from the difficulty of extracting the rich information contained in waveforms. To address this, we employ summary statistics that compress the data while preserving information needed to infer unknown subsurface properties. Summary statistics can either be hand-crafted by domain experts or learned by exploiting probabilistic symmetries within the data (Bloem-Reddy et al., 2020). In this work, we follow the methods of Orozco et al. (2023) and Yin et al. (2024b) by using physics-based summary statistics derived from the physical forward operator. Specifically, we utilize the gradient of the data likelihood, which allows us to inject physics into the generative process at the cost of a single PDE solve per set of posterior samples, where the PDE corresponds to the computations required for a single migration.

Using this gradient serves as a natural way to undo the complexity of the waveforms since it brings the data into the model space. Theoretically, this approach is well-founded, as it optimally saturates the information inequality (Alsing and Wandelt, 2018), a bound that limits how much information a summary statistic can extract about an unknown variable. Empirical results have shown that incorporating these summary statistics accelerates training and improves convergence with fewer data samples (Orozco et al., 2023). Given an observation \mathbf{y} and a migration-velocity model \mathbf{x}_0 , the summary statistic is calculated as follows:

$$\overline{\mathbf{y}} := h(\mathbf{y}) = \overline{\nabla \mathcal{F}}(\mathbf{x}_0)^{\top} (\mathcal{F}(\mathbf{x}_0) - \mathbf{y}), \tag{4}$$

where $\overline{\nabla \mathcal{F}}$ is the subsurface-offset extended Jacobian, following the method of (Hou and Symes, 2016; Yin et al., 2024b). $\overline{\mathbf{y}}$ contains the CIGs, which represent the summarized waveform but transformed to model space, while preserving more information compared to RTMs in situations where the migration-velocity model is poor. We summarize all training data $\overline{\mathbf{y}}^i = h(\mathbf{y}^i)$ and form a new training dataset $\overline{\mathcal{D}} = \{\mathbf{x}^i, \overline{\mathbf{y}}^i\}_{i=0}^N$ and train a conditional Diffusion network with Equation 3. At inference time, the observation \mathbf{y}^{obs} is summarized in the same manner, $\overline{\mathbf{y}}^{\text{obs}} = h(\mathbf{y}^{\text{obs}})$ and then passed into the same sampling process as Equation 2. The computational cost of this approach is low because it requires only a single extended migration per observation at inference time, making it more computationally efficient than non-amortized methods that typically demand hundreds of PDE solves (Zhao et al., 2022) for each dataset. Our approach is also amortized and therefore can be applied to many unseen observations without repeating the costly training process.

6. Stylized examples

We separate our experiments into two parts. First, we train our generative networks on synthetic seismic model sets and validate them on unseen datasets

from the same synthetic distribution as used during training. Secondly, we apply these trained networks to field datasets to assess their robustness in practical scenarios and also to understand the prior that they learn.

6.1. Training dataset generation

For the synthetic experiments, the migration-velocity models used are intentionally not kinematically accurate. For the two salt imaging experiments, we first remove the salt body from the model, replace it with the average velocity of the sedimentary layers, and then smooth the resulting model using a Gaussian kernel. To minimize artifacts from tomographic updates, the migrations are generated using the inverse-scattering imaging condition (ISIC) (Witte et al., 2017), which implies that our method is purely reflection-based. The sources are given by Ricker wavelets that are filtered to remove unrealistically low frequencies below 3 Hz. When noise is added to the simulated shot gathers, we apply a filter to ensure the noise contains the same frequency content as the source wavelet. We use JUDI and Devito for wave simulations [Witte et al. (2017); Louboutin et al. (2019); Luporini et al. (2020);]. The extended Jacobian operator was created using (Louboutin, 2024) with a subsurface range that was chosen to contain the majority of the non-zero offset energy.

Across all experiments, we create between 700°800 training pairs. The Diffusion networks are trained until the image quality metrics (RMSE, SSIM) for the posterior means stop improving on a validation set held out during training. To calculate posterior statistics, we generate N posterior samples and calculate Monte Carlo estimations of the posterior mean, $\mathbf{x}_{\text{mean}} = \sum_{i=0}^{N} \mathbf{x}_{\text{post}}^{i}/N$, and standard deviation, $\mathbf{x}_{\text{std}} = \sqrt{\sum_{i=0}^{N} (\mathbf{x}_{\text{post}}^{i} - \mathbf{x}_{\text{mean}})^{2}/N}$. The number of posterior samples to use is decided by increasing the number until the posterior standard deviation converges; in our case, N = 64.

6.2. Compass model

Our evaluation begins by using the Compass model (Jones et al., 2012). The training dataset consists of the same velocity and CIGs pairs as in WISE (Yin et al., 2024b). These include N=800 training pairs of velocity models of size (512 × 256) that are discretized with 12.5 m and CIGs that are generated with 50 equally spaced offsets between -500 m to 500 m without ISIC. The migration-velocity models for the Compass dataset are created using a single 1D velocity profile that is derived from the training dataset. Our only modification is that we use conditional Diffusion as the generative network instead of conditional normalizing flows. Training took 14 GPU hours, while posterior sampling takes 440 sec for the 64-shot CIGs in addition to 2 sec for each posterior sample. The results summarized in Figure 1 confirm the observation from Yin et al. (2024b) that CIGs drastically improve posterior sampling performance. As we discuss later, these results improve on the normalizing flow results from Yin et al. (2024b). Overall, we observe increasing error and uncertainty with depth. Additionally, there is correlation between the complexity of the velocity model

and the error and uncertainty. Aside from uncertainty near the strong lateral variation along the major unconformity in the model, we also observe increased errors and uncertainty associated with topology on the velocity kickback that occurs around 750 m depth on the left side of the model. In the section on uncertainty benchmarks, we expand this rudimentary analysis and detail how we can determine which uncertainty is of higher quality according to well-defined metrics.

6.3. Synthoseis models

While the results presented in the previous section are encouraging, the geological setting in the North Sea Compass dataset lacks sufficient complexity to put our inference methodology to the test. In addition, its training was limited to neighboring 2D slices from the same area and therefore may lack in diversity. To address this potential lack of diversity and complexity, we consider an example where we train on synthetically generated models produced by the opensource software package Synthoseis[https://github.com/sede-open/synthoseis]. Synthoseis is an algorithm designed to generate realistic and diverse synthetic 3D seismic models tailored for deep learning applications (Merrifield et al., 2022). Our approach specifically uses the algorithm's velocity-model generation routines, focusing on the creation of the acoustic velocity property (V_n) of Earth models. The workflow consists of several key steps, namely initialization of random Earth parameters ranges, generating 3D depth horizons, embedding of rock property models, and ultimately producing 3D volumes. In this study, we examine scenarios with Earth models that feature salt bodies. Although each model produced by the algorithm exhibits full 3D structures, for our experiments, we extracted 2D slices from the 3D models to manage computational resources needed during Synthoseis generation. It is important to note that while these models are not created by the same generative model that we train, thus using these samples does not fall under the regime of autophagy as defined in (Alemohammad et al., 2023).

To create the training dataset $\overline{\mathcal{D}}$, we generate N=800 pairs. Each \mathbf{x} has a grid size of 512×256 with a spatial discretization of 12.5 m. We modeled towed sources at the ocean surface with an interval of 12.5 m. The receivers are placed on the ocean bottom with an average sampling of 200 m, they are positioned using a random jittered sampling scheme (Hennenfent and Herrmann, 2008). The shot records \mathbf{y} are simulated by recording for 3.2 s, while the active sources are modeled with a Ricker wavelet with central frequency of 20 Hz. The simulated noise was band-limited to contain the same frequency content as the source and had a magnitude of 25 dB. To make migration-velocity models, we first replace values where salt is located with the average value of the sedimentary layers. Then, we convert the model from depth to time, smooth in time with an anisotropic Gaussian kernel of size (40×80) , and then convert it back to depth. We follow this nonlinear procedure to intentionally create poor migration-velocity models. The horizontal subsurface-offset migrations $\overline{\mathbf{y}}$ include 24 equally spaced offsets between -500 m and 500 m. The conditional Diffusion network was trained

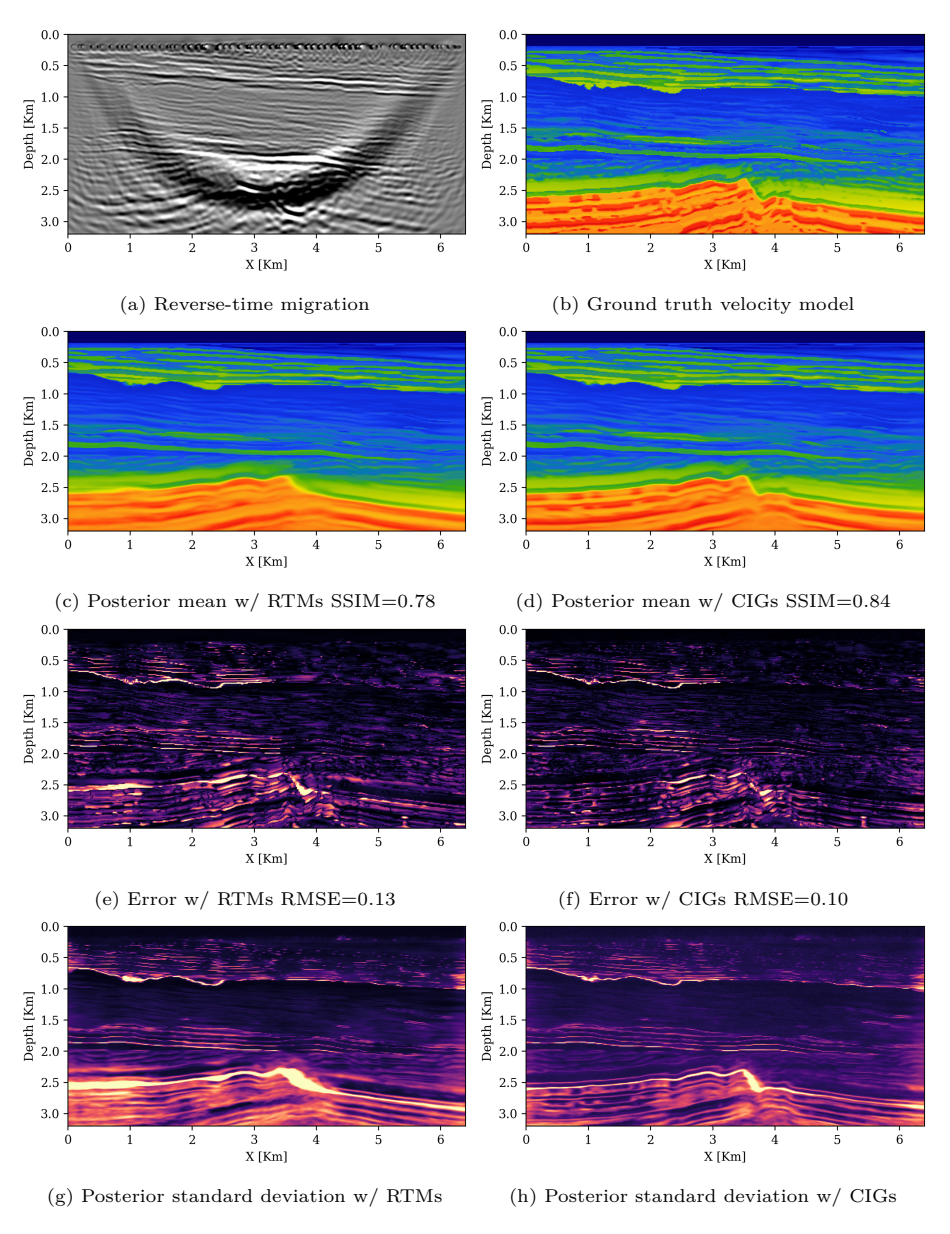


Figure 1: Posterior sampling on Compass dataset. We observe an increase in quality of the inferred velocity model when using CIGs instead of RTMs.

for 12 GPU hours. For inference, the algorithm takes 277 sec to generate CIGs for 32 shots and 2 sec for each posterior sample.

After training, we consider an example not seen during training for posterior sampling. The results are shown in Figure 2. Our first observation is that, over both image quality metrics (SSIM and RMSE) the network trained with CIGs outperforms the network trained on RTMs only. Furthermore, we are pleased that although there is uncertainty below the salt structure, as evidenced by the high standard deviation Figure 2i,Figure 2j and posterior means Figure 2e,Figure 2f that appear blurred in regions where the uncertainty is large, the individual posterior samples in Figure 2c,Figure 2d exhibit an accurate approximation of the prior in the way the salt is sharply delineated. As before, the posterior mean \mathbf{x}_{mean} and posterior standard deviation \mathbf{x}_{std} are calculated from 64 posterior samples. Again, we see reasonably good correlation between the errors and uncertainty where as expected, these occur mainly at the bottom of the salt and in the subsalt areas. It is also encouraging that the unlapping sedimentary layers are well recovered albeit the inference struggles in the area beneath the deepest point of the salt.

6.4. Quantitative assessment of UQ

Evaluating the quality of the UQ—i.e., quality of the inference of the posterior, from posterior samples is crucial for understanding how well the network captures the true variability in the posterior distribution. In this section, we introduce four approaches to assess the performance of UQ, namely (1) the ability to warn areas with high error; (2) the degree of correlation between uncertainty and error; (3) the posterior coverage, which is defined as the proportion of pixels for which the range of posterior samples contains the ground truth; and (4) the ability of posterior samples to fit the observed shot data. For all metrics, we take the uncertainty to be the standard deviation between posterior samples and the error calculated between the posterior mean and a known ground truth velocity model.

6.4.1. Percentage of regions with large errors but low uncertainty

An important feature of UQ is its ability to warn the user of areas that may have high errors in the reconstruction. By warning, we mean that if an area has high uncertainty, then that area should have high error. Thus, we want to avoid high errors that are not followed by high uncertainty, which could be an indication of poor UQ. To quantify and visualize this, we use the z-score as defined (Wu et al., 2024) by the pixel-wise division of the error by the uncertainty: z-score = $|\mathbf{x}^* - \mathbf{x}_{\text{mean}}|/\mathbf{x}_{\text{std}}$ where \mathbf{x}^* is the ground truth velocity, \mathbf{x}_{mean} the average of the posterior samples, and \mathbf{x}_{std} their pixelwise standard deviation. In Figure 3, we show that high errors are "acceptable" as long as it is followed by high uncertainty in that same area, while areas with high errors and low uncertainty will have high values for the z-score in this plot. To highlight these areas, grid points with errors that are $2\times$ larger than the uncertainty are shown in red.

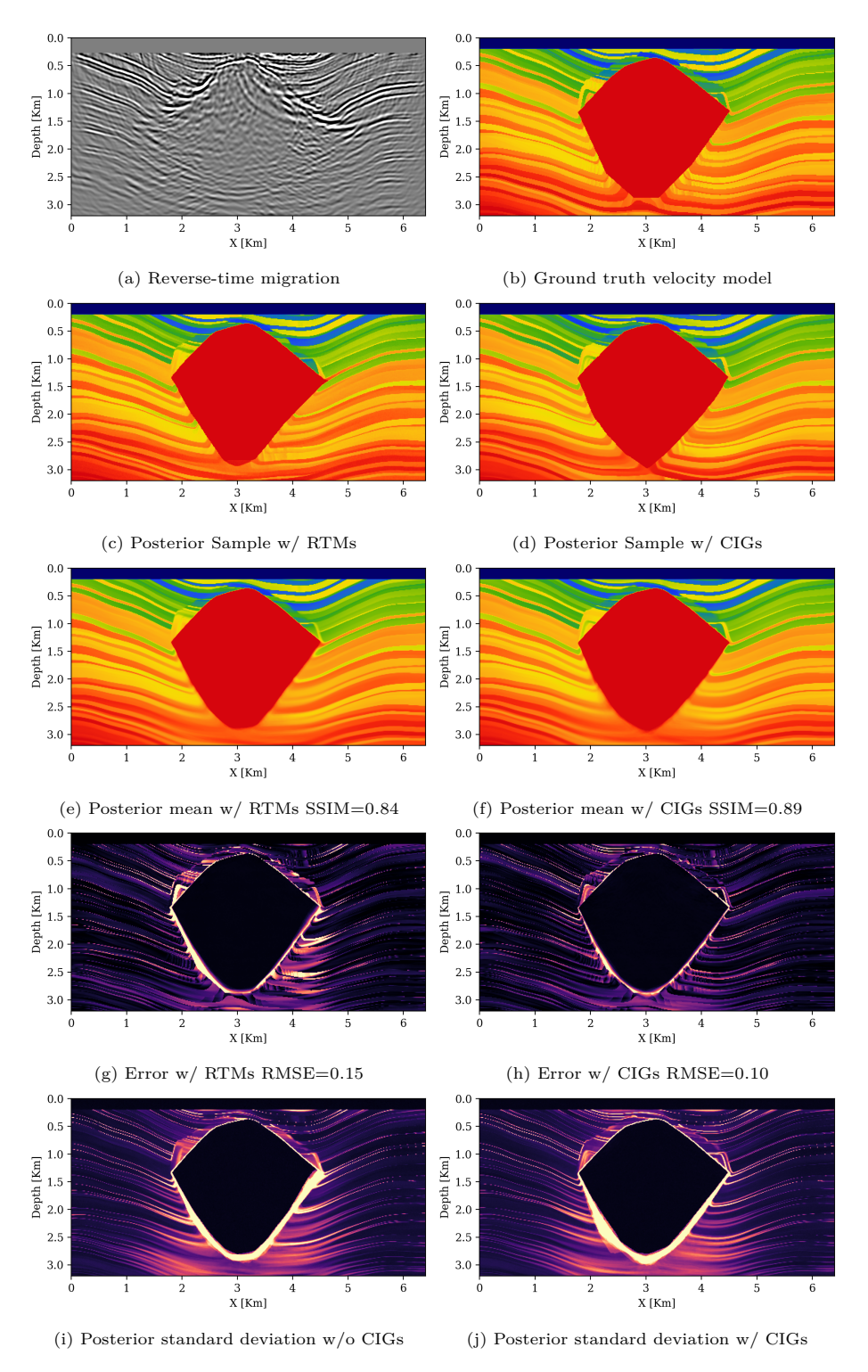


Figure 2: Posterior sampling on velocity models generated by Synthoseis. Based on the image quality metrics, the CIGs more accurately inform the posterior inference.

To ensure good UQ, we want to minimize the total red area. Thus, we define the quantitative metric as the percentage of pixels that are red and aim for this metric to be low. In Table 1, we show the average z-score percentage over posterior sampling results of 50 test unseen observations for both RTMs and CIGs trained networks. From Figure 3 we make the following observations: for both models, the total area of the red regions is significantly smaller when the posterior is conditioned on CIGs. We also observe that red regions for the Compass model tend to be associated with areas where the velocity kickback exhibits lateral variations. With few exceptions, we see that red regions for the salt models generated by Synthoseis are located near steeply dipping events. Overall, percentages of red area are significantly reduced thanks to the use of CIGs.

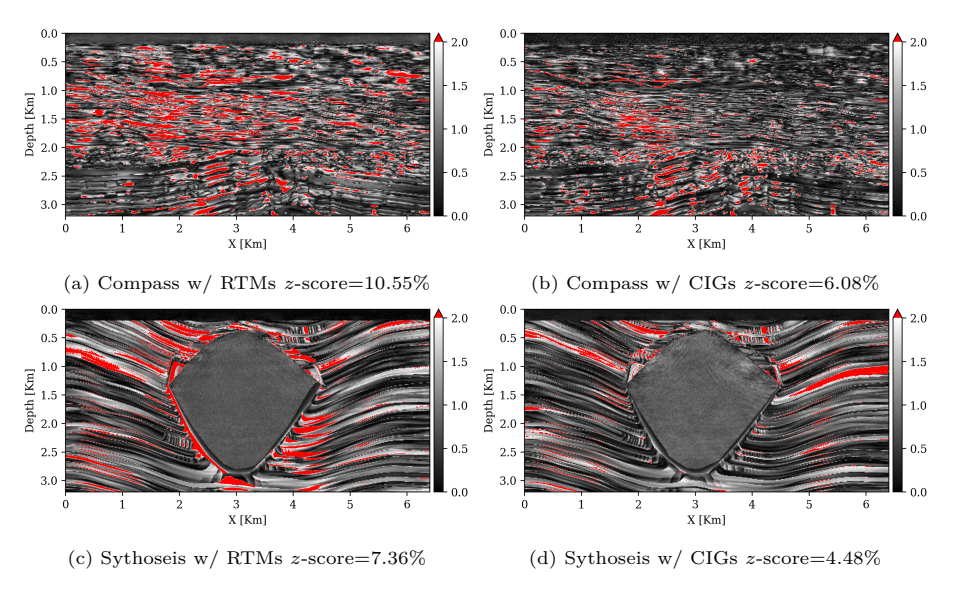
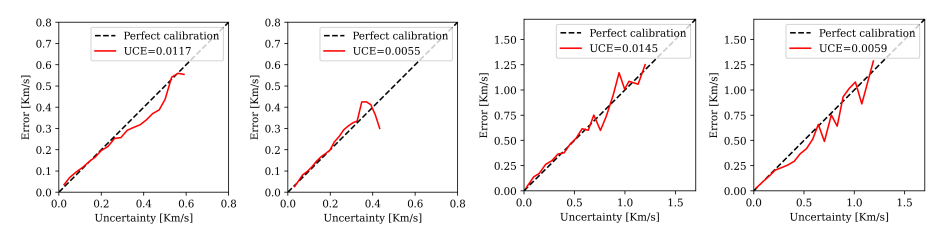


Figure 3: Comparison of the z-score between conditional Diffusion networks trained on RTMs and networks trained on CIGs with 24 non-zero offsets. We desire the z-score (percentage of pixels where error is $2 \times$ higher than UQ) to be low.

6.4.2. Degree of calibration

While correctly warning of high errors is an indication that the UQ is reasonable, it does not provide a precise quantitative metric for the correspondence between error and UQ at various magnitudes. For this purpose, we use the calibration test from (Laves et al., 2020; Guo et al., 2017) to quantify the correlation between predicted uncertainty and error. By binning the pixels over different magnitudes, we can build a correlation plot wherein we want pixels that are placed into bins of certain errors magnitudes to have similar uncertainty magnitudes. Figure 4 shows the application of this test to the UQ results for the Compass example in Figure 1 and the Synthoseis example in Figure 2. The uncertainty calibration error (UCE) is a single scalar summarizing the performance of this test by

calculating the area between the red curve and the optimal calibration on the diagonal dashed line. Therefore, lower UCE values indicate better-calibrated uncertainty. Again, we observe major improvements due to the use of CIGs for both models. In Table 1, we show the average UCE for posterior sampling results on 50 unseen test observations for both RTMs and CIGs networks.



(a) Compass w/ RTMs (b) Compass w/ CIGs (c) Synthoseis w/ RTMs (d) Synthoseis w/ CIGs

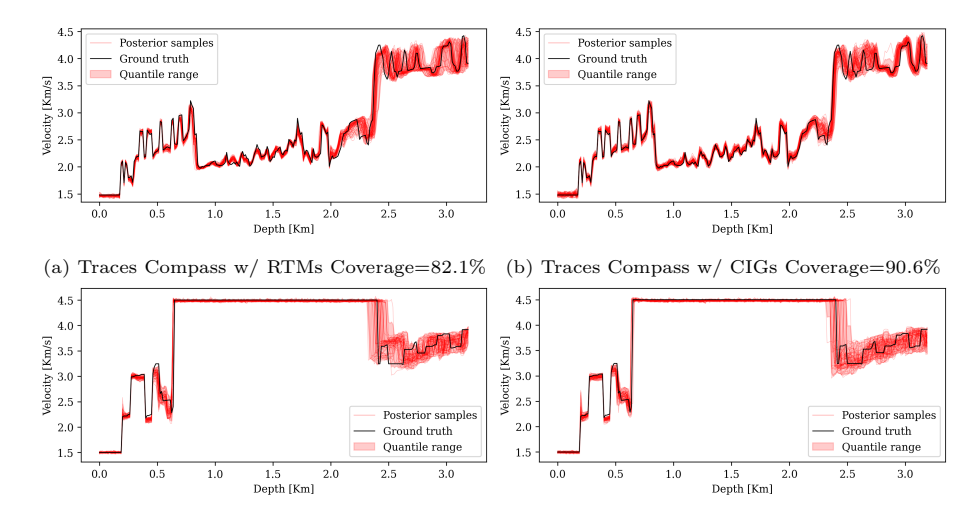
Figure 4: Comparison of the uncertainty calibration of a conditional Diffusion network trained on RTMs compared with network trained on CIGs with 24 non-zero offsets. For both synthetic datasets, the CIGs trained network is better calibrated as evidenced by the lower UCE metric.

6.4.3. Posterior coverage percentage

Next, we quantitatively evaluate the coverage of the posterior samples. Coverage measures whether the true velocity model is contained within the spread of the posterior distribution. This is an important characteristic of Bayesian methods, as we want the ground truth velocity model to be included within the posterior samples (Tachella and Pereyra, 2023). To quantify coverage in percentages, we compute the lower and upper percentiles of the posterior samples at each pixel and test if the ground truth velocity model is contained within that range. The quantified metric corresponds to the percentage of pixels for which the calculated range contains the ground truth velocity model. Ideally, this coverage percentage should be high. Visually this test is intuitively understood in Figure 5 where we plot samples of the posterior over a single vertical trace and compare them with the ground truth velocity. For our metric, we calculate the range using the upper 99% and lower 1% percentiles. Although we only show a trace in these figures, note that the coverage metric is calculated over all pixels in the reconstructed velocity models. In Table 1, we include the average coverage percentage over 50 test samples for both RTMs and CIGs trained networks. We want this metric to be high because we wish our posterior distribution to always contain the ground truth velocity model.

6.5. Shot data residual of posterior samples

Even though the above quantitative assessment of UQ is valuable, it relies on having access to ground truth velocity models rendering these metric impractical for field data where the ground truth velocity models are unknown. For this reason, it is as a final check important to make sure that the proposed velocity-model inference produces synthetic gathers that fit observed shot gathers. In other words, while the generative samples \mathbf{x}_{post} shown previously seem to visually



(c) Traces Synthoseis w/ RTMs Coverage=87.0% (d) Traces Synthoseis w/ CIGs Coverage=89.7%

Figure 5: Vertical traces through the posterior samples and the ground truth velocity model used to calculate the posterior coverage metric.

match the correct prior, we will verify that these are indeed Bayesian and respect the data likelihood $p(\mathbf{y} \mid \mathbf{x})$. We take the posterior samples and pass it through the nonlinear forward wave operator $\mathcal{F}(\mathbf{x}_{\text{post}})$ and analyze the fit to the observed shot data \mathbf{y}^{obs} . In Figure 6, we show a pairwise binned comparison between the predicted and observed shot gather interleaved with increasing receiver coordinate. To quantify the fit, we take the division between the noise norm and the data residual that we define as $\|\boldsymbol{\varepsilon}\|_2/\|\mathcal{F}(\mathbf{x}_{\text{post}})-\mathbf{y}^{\text{obs}}\|_2$ and report this number as a percentage. With 100% corresponding to the residual having the same normed magnitude as the noise, in other words, a perfect fit. For both models, the network conditioned on the CIGs better fits the shot gathers.

Results of the four performance metrics: (1) percentage of regions with large errors, (2) degree of calibration, (3) posterior coverage percentage, and (4) posterior fit of shot data are included in Table 1 for networks trained with RTMs or CIGs. From these results, we conclude that conditioning on CIGs improves performance with respect to RMSE and SSIM for the recovery results themselves, and with respect to these four metrics that reflect the quality of the UQ. This improvement is due to the CIGs containing more information than the RTMs, even in situations where the migration-velocity models are poor. As a result, CIGs provide a more accurate representation of the original posterior that is conditioned on raw shot records.

We include the performance on the same Compass dataset used in (Yin et al., 2024b), showing that our Diffusion network with average SSIM of 0.85 outperforms the normalizing flow, which had an average SSIM of 0.63 (Yin et al., 2024b). While this increase in performance is encouraging, we cannot definitively

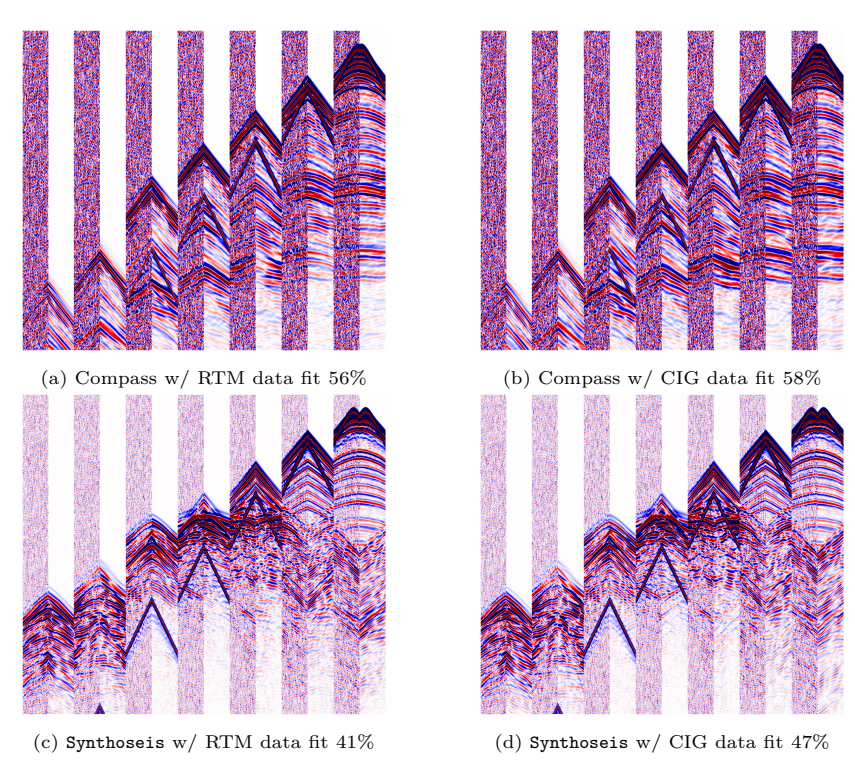


Figure 6: Interleaved comparison between paired bins of observed and synthetic shot data.

conclude that Diffusion is in general better than normalizing flows since our Diffusion network uses different architectures than the normalizing flow in (Yin et al., 2024b) and also has more training costs. A careful comparison between these two frameworks is beyond the scope of this paper but would be a valuable avenue for future work.

Table 1: Image and uncertainty quality metrics on Compass and Synthoseis datasets.

Dataset	RMSE ↓	SSIM ↑	Coverage [%] ↑	UCE ↓	z -score [%] \downarrow	Data fit [%] ↑
Compass w/o CIGs	0.12	0.81	73.8	0.013	10.7	53.7
Compass w/ CIGs	0.11	0.85	74.8	0.011	9.9	54.2
Synthoseis w/o CIGs	0.085	0.91	72.5	0.012	7.8	77.1
Synthoseis w/ CIGs	0.079	0.92	74.6	0.009	5.4	79.6

7. Complex case studies

So far, the stylized examples have exhibited relatively minor complexity, which in part explains the success of the inference discussed so far where the reconstructed velocity models significantly bring down the residuals. Due to the the always present amortization gap (Marino et al., 2018; Orozco et al., 2024), which corresponds to a drop in accuracy due to an attempt to generalize the performance of the network over many velocity models instead of focusing the inference on a single shot dataset as in non-amortized methods (Zhao et al., 2022; Siahkoohi et al., 2023; Izzatullah et al., 2024), we cannot expect the presented amortized approach to perform well on larger models with increased geological complexity. Using an example involving the SEAM salt model (Fehler and Keliher, 2011), we demonstrate how our inference approach can be extended to handle complex salt plays. Finally, we also consider a field dataset to demonstrate the importance of having access to relevant training data.

7.1. Salt flooding with ASPIRE

To ameliorate the amortization gap and to accommodate complexities arising from salt in the Gulf of Mexico, we adapt and extend methodologies introduced by Orozco et al. (2024) and retrain the networks at the next iteration on migrations improved by the average of the posterior samples produced by the current iteration. This type of approach, known as ASPIRE (Orozco et al., 2024), which can be interpreted as a probabilistic loop-unrolled gradient descent algorithm (Putzky and Welling, 2017; Gregor and LeCun, 2010), remains amortized and has been demonstrated to close the amortization gap in transcranial ultrasound

brain imaging. Motivated by these findings, and by the fact that ASPIRE lends itself well to iterative workflows, we propose a methodology aimed at improving the large data residuals observed in Figure 7a. These residuals are mainly due to the complexity of the velocity model and the lack of training data, a situation where amortized methods are known to fail (Siahkoohi et al., 2023; Orozco et al., 2024).

To remedy this situation and decrease the data misfit, we follow ASPIRE and produce an improved migration-velocity model based on the average of the posterior samples. With this improved velocity model, new CIGs $\overline{\mathbf{y}}_1$ are computed, as in Equation 4, but now with \mathbf{x}_{mean} —i.e., the posterior mean, serving as the migration-velocity model instead of \mathbf{x}_0 . After calculating CIGs for each training sample, we train a new network on the updated dataset $\overline{\mathcal{D}}_1 = \{\mathbf{x}^i, \overline{\mathbf{y}}_1^i\}_{i=0}^N$. While this choice of posterior mean (e.g. as opposed to posterior median) is still open to debate, Orozco et al. (2024) proved that it leads to significant improvements. Although there are additional offline and online costs associated with this method, the inference stage remains relatively computationally efficient with the cost of a single migration per iteration and a low total number of iterations, in this case two iterations.

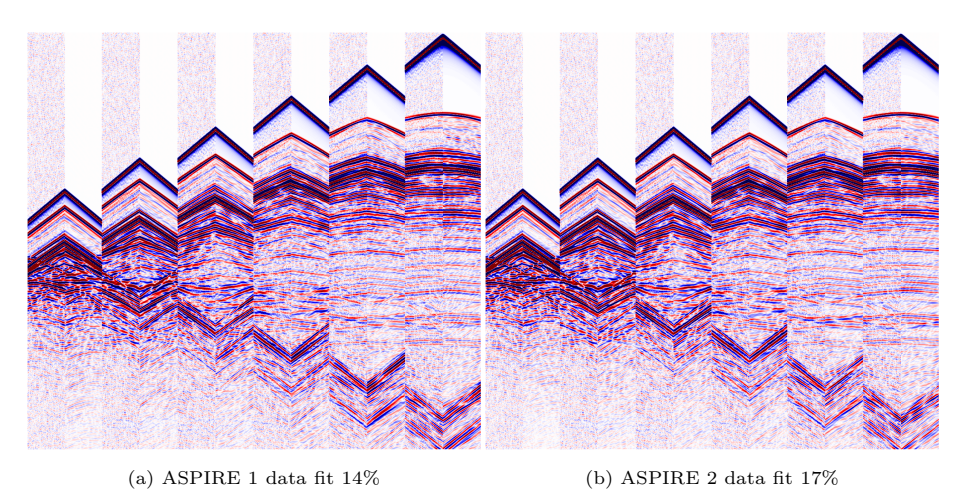


Figure 7: Comparison of data misfit of a shot record generated from the posterior samples for two ASPIRE iterations by interweaving traces from the observed shot and simulated shot gathers. The second ASPIRE iteration has improved the data fit by using one more gradient (extended migration) at test time.

7.1.1. Experimental setup

To demonstrate how inference with ASPIRE can be adapted to complex settings, we consider 2D slices through the 3D SEAM model (Fehler and Keliher, 2011), which represents complex salt geometry typical for the Gulf of Mexico. We create a training split of the SEAM model by selecting a continuous subset of crosslines for training. To avoid similarity between 2D slices, we skip 2 km between the

nearest training slice and the nearest test slice.

When simulating shot gathers, we generate narrow-offset 2D seismic lines with a grid size of 1744×512 and a spatial discretization of 20 m. A marine dataset is created by simulating shot data with sources and receivers towed at the same depth near the surface. Surface-related multiples are avoided by applying an absorbing boundary condition at the surface. Computational costs are reduced by using a coarse source interval of 1000 m, while receivers are sampled at 20 m and a maximum offset of 6 km. The total recording time for each shot record is 9 s, and Gaussian noise is added to yield a level of 25 dB in a frequency band that matches the source signature. With these settings, 32 shots were simulated for a model with constant density and varying velocity.

Migration-velocity models are created by first removing the salt from the ground truth velocity models, followed by smoothing the result with a Gaussian kernel of grid size 25 (see Figure 8). To capture most of the energy, the horizontal subsurface-offset migration utilizes 50 equally spaced offsets, ranging from -2000 m to 2000 m. After imaging the full seismic line, we extract subsets to create the training pairs by taking sliding windows of each 2D line, resulting in grids of size 512×512 and a total of 700 training data pairs. Each ASPIRE iteration takes 12 GPU hours to train. While the conditional Diffusion network is trained on these smaller patches, at inference time the trained network is evaluated on the full grid size of (512×1744) . This is feasible because our Diffusion network predominantly relies on convolutional layers, allowing for evaluation on grid sizes larger than those used during training. At inference, we incur the cost of one extended migration (3 min) per ASPIRE iteration and then 8 sec per posterior sample.

7.1.2. Algorithmic innovations

To successfully adapt ASPIRE to the complex setting of SEAM, the following innovations are implemented:

- Utilization of previous iterates. In its vanilla implementation, gradient descent and, therefore ASPIRE, base its updates on gradients taken at the current model iterate (read inferred velocity model), ignoring information from previous iterates. Motivated by quasi-Newton optimization methods, Putzky and Welling (2017) proposed to add previous model iterates to improve convergence and approach reminiscent of quasi-Newton methods where previous gradients are used to approximate the Hessian. Similarly, we allow the networks at each iteration to take all previously calculated CIGs and inferred migration-velocity models as input. In our experiments, including this modification significantly improved the performance of ASPIRE.
- Incorporation of domain knowledge with salt flooding. To detect the bottom of the salt, we employ the well-established method of salt flooding (see Esser et al. (2016) and the references therein) during which top salt is extended downwards. Due to its iterative structure, ASPIRE

can easily accommodate salt flooding, so the bottom of the salt is clearly delineated by migration on the second iteration.

7.1.3. Preliminary results

In Figure 8, we present the results from two iterations of ASPIRE, starting from the smoothed migration-velocity model depicted in Figure 8a. This migrationvelocity model is used to produce the initial CIGs, whose zero-offset section is displayed in Figure 8b. Based on these CIGs, the first trained ASPIRE produces posterior samples, whose average is plotted in Figure 8c. While the top of salt is well recovered, comparison with the ground truth velocity model depicted in Figure 8h shows that important details are missing in the bottom salt. This, in turn, leads to poorly resolved bottom salt in the zero-offset migrated section Figure 8d. By flooding the salt downwards, as depicted in Figure 8e, this issue is largely mitigated, as observed from the migration included in Figure 8f, where the bottom salt is delineated sharply and includes the main topological features. This means that the second trained ASPIRE on salt-flooded migrations can correctly infer the salt bottom as shown in Figure 8g. Before comparing the migration in this model to a baseline derived from the true model, let us first consider the contraction of the inferred uncertainties resulting from the ASPIRE iterations.

In addition to providing increasingly better estimates for the velocity model, ASPIRE also includes UQ at each iteration. In Figure 9, different aspects of the inferred uncertainties for ASPIRE 1 and 2 are illustrated by means of plots for errors included in figures 9a and 9b; posterior standard deviation in figures 9c and 9d; z-score in figures 9e and 9f; and finally plots for the coverage in figures 9g and 9h. From these plots, the following observations can be made: First, errors with respect to the ground truth velocity model at the bottom salt are greatly reduced by ASPIRE 2 due to the salt flooding. However, errors remain at both ends of the salt due to a lack of illumination. As expected, errors remain in the sediments below the salt. Second, as expected, predicted uncertainties at the bottom salt are reduced for ASPIRE 2 (see figures 9c and 9d). The uncertainty also correlates reasonably well with the errors. We also observe the appearance of dirty salt, which can be explained by the fact that the salt in the SEAM dataset includes dirty salt. Third, with very few exceptions there is a drastic improvement in the overall z-score plots (figures 9e and 9f) for ASPIRE 2. Most notably, z-scores improve significantly at the bottom-salt interface and within the sedimentary layering under the salt. Finally, the coverage of the posterior samples is also improved. While the ground truth bottom salt was missed in ASPIRE 1, the posterior samples yielded by ASPIRE 2 clearly contain the step-out of the salt.

Moreover, visual improvements in the second ASPIRE iteration are supported by quantitative uncertainty quality measures listed in the captions of Figure 9 and in Table 2, summarizing performance over eight unseen test 2D lines. Overall, the progression of results correlates well with the iterative focus of ASPIRE: the first iteration targets the top of the salt and the second iteration targets the

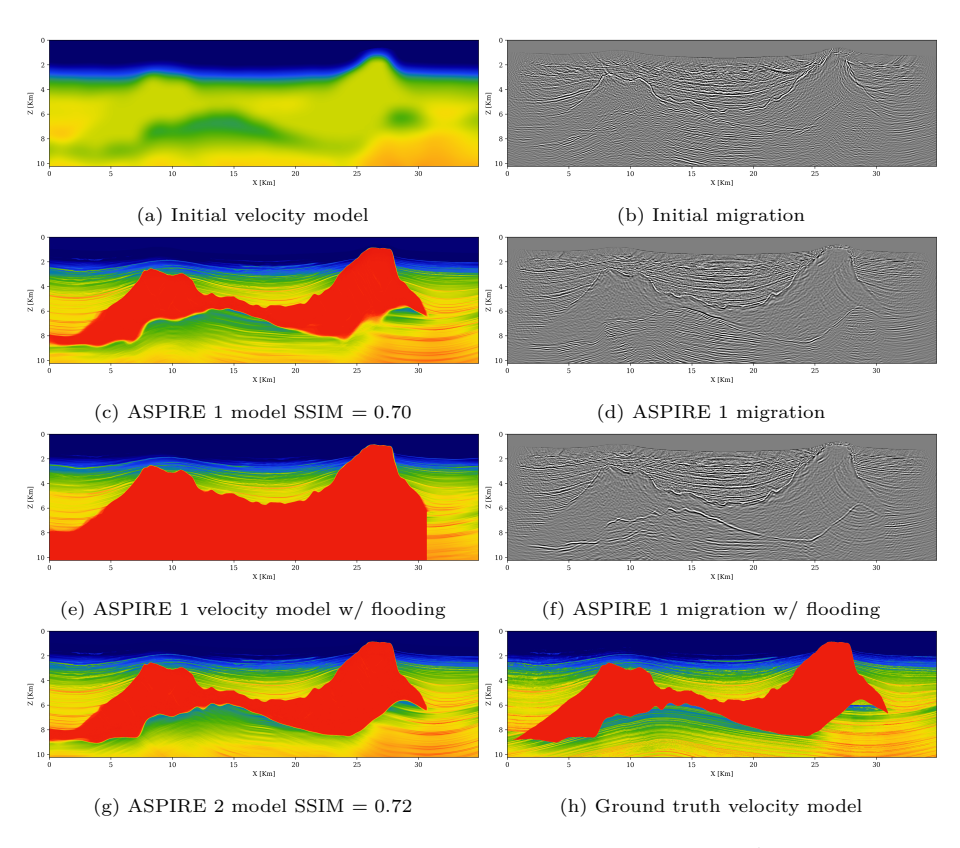


Figure 8: Comparison of posterior means yielded by two iterations of ASPIRE and their corresponding reverse-time migrations.

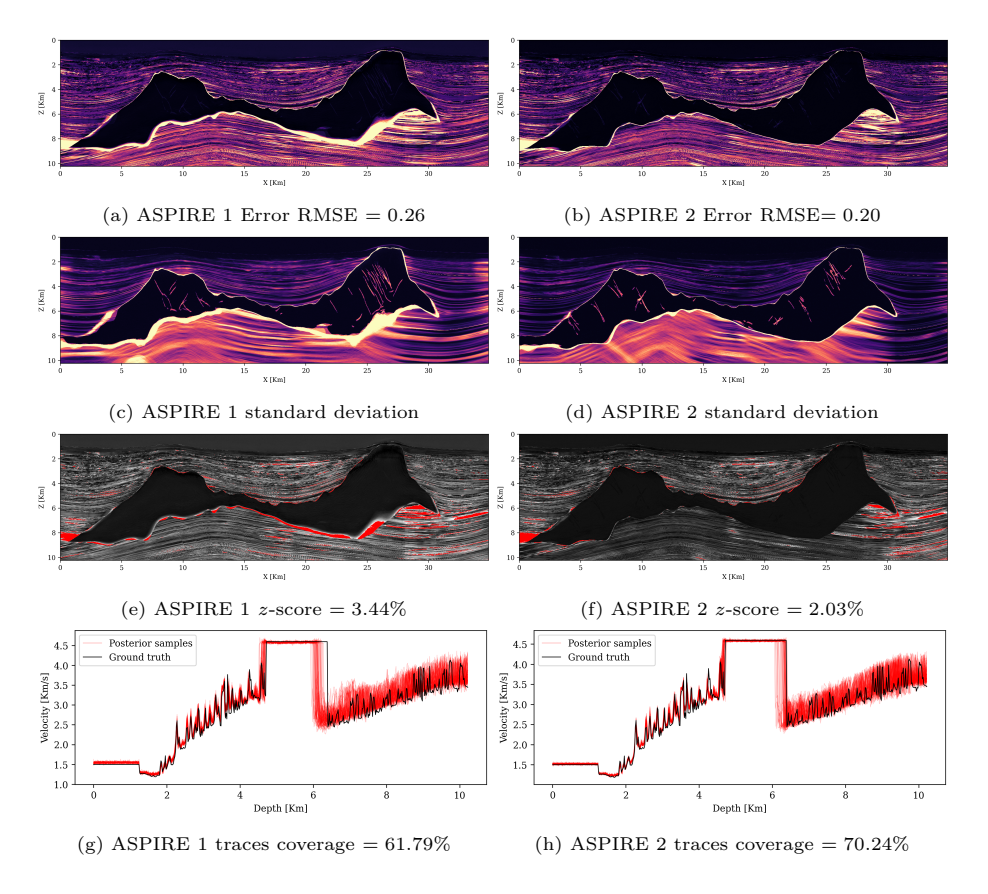


Figure 9: Comparison between recovery and UQ quality yielded by ASPIRE 1 and 2.

bottom of the salt. The corresponding shot gathers for the different ASPIRE iterations are included in Figure 7 and confirm that the model improvements lead to improved data fit.

Table 2: Image and uncertainty quality metrics on SEAM dataset ASPIRE iterations.

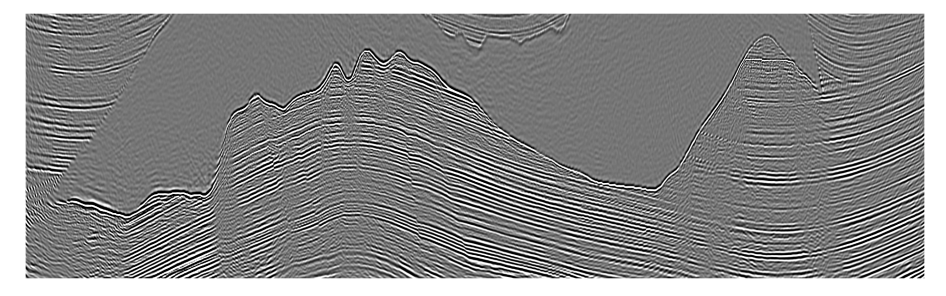
Dataset	$\mathrm{RMSE}\downarrow$	SSIM ↑	Coverage [%] ↑	UCE ↓	z -score [%] \downarrow	Data fit [%] ↑
ASPIRE 1	0.25	0.71	66.6	0.043	3.44 3.96	13.3
ASPIRE 2	0.21	0.73	67.3	0.042		15.5

7.1.4. Quality assessment

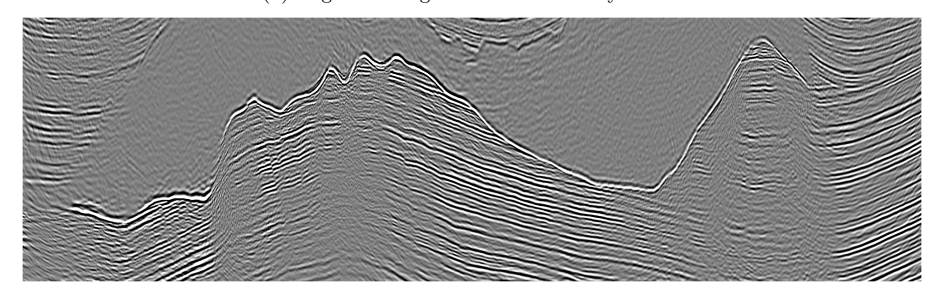
While the recovered velocity models and uncertainty quality metrics show significant improvements between ASPIRE 1 and 2, the ultimate goal is to assess the impact of these improvements on the final product, namely, the migrated image in areas below the salt. For this purpose, we included Figure 10, which contains results of RTM with the ground truth velocity model; the mean of reverse-time migrations carried out in 16 posterior samples for the velocities produced by ASPIRE 2; error with respect to the migrated image with the ground truth velocity model; and the standard-deviation of reverse-time migrations in posterior velocity models. From these plots, the following observations can be made: First, the migrations in the ground truth velocity model and the inferred mean of the multiple RTMs are close, even though issues remain. These include: errors in the delineation some areas of bottom salt and minor shifts in imaged sedimentary layers below the salt. While there are errors, we emphasize that errors are expected to occur in this ill-posed problem, but that our solution comes with uncertainty quantification that powerfully points to areas of error (see figures 10c and 10d). We observe that the predicted uncertainty is overly cautious, predicting larger variability than evidenced in the plot of errors with respect to the migration with the ground truth velocity model. We consider the fact that uncertainty being overestimated as advantageous since it offers an additional safeguard to overinterpretation of imaged reflectors as opposed to being overconfident. Both migrations suffer from an overprint due to areas of relatively poor illumination due to the interplay between small offsets and complexity of the salt geometry, which gives rise to (de)focusing effects that explain variations in the amplitudes of the imaged reflectivity under the salt.

7.2. Field data proof of concept

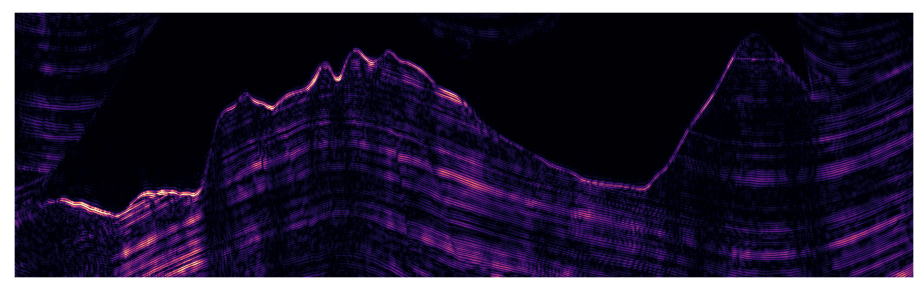
Our aim is to develop ML-enabled workflows for probabilistic velocity model building capable of scaling to industry-sized seismic datasets. To demonstrate progress and challenges toward this goal, we apply the same approach with pre-trained networks from the previous experiments to a large shallow-water seismic 2D line. The aim of this exercise is twofold: First, we aim to demonstrate



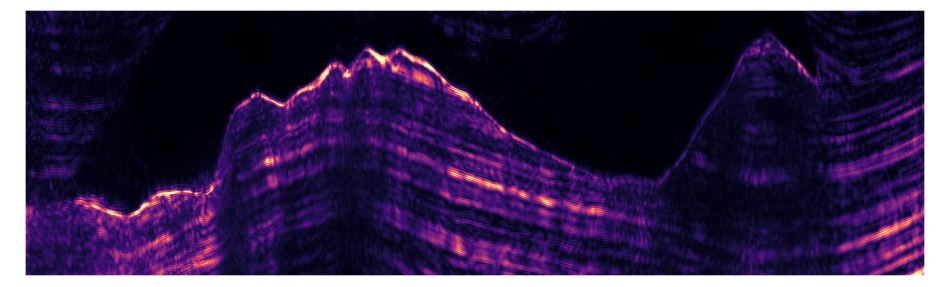
(a) Migration in ground truth velocity model



(b) Mean of migrations in velocity models produced by ASPIRE 2 $\,$



(c) Error between mean of migrations in velocity models produced by ASPIRE 2 and ground truth migration



(d) Standard deviation of migrations in velocity models produced by ASPIRE 2 $\,$

Figure 10: The migration in our final velocity model is close to the migration in the ground truth model.

that the presented methodology can be applied to field data. Second, we aim to showcase the main limitations of the presented approach—i.e., its reliance on training datasets that are pertinent to the geological setting under consideration.

7.2.1. Shallow-water field data

We thank Woodside Energy Group for providing access to the dataset referred to as "Galactic 2D", made available under Creative Commons BY-SA 4.0 licence [https://creativecommons.org/licenses/by-sa/4.0/] as part of Phase 2b of the 2023 Galactic 2D Seismic Imaging Study. We have not made any modifications to the original work. We consider the migration and velocity models derived from "Galactic 2D". These derivatives are obtained with a traditional workflow, consisting of migration-velocity building with FWI and RTM, as shown in figures 11a and 11b.

The 2D line of the Galactic dataset being considered has a grid size of (512×7024) . To produce samples, the migration shown in Figure 11b served as input to conditional neural networks trained on velocity models from the Synthoseis and SEAM datasets. In this case, we trained a network on Synthoseis samples that did not contain salt. Since the Galactic dataset does not include non-zero offset migrations, we use the RTM included in Figure 11b as input, producing the posterior means shown in figures 11c and 11d. For this large line, each posterior sample takes 30 seconds to generate. Both estimates are obtained from 64 samples of the posterior.

The posterior mean estimates produced by either network do not seem realistic because they are strongly biased toward the datasets these networks were trained on. The fact that the result obtained with Synthoseis looks more reasonable likely stems from the fact that Synthoseis dataset contains more variability in its training set. Still, this example underlines the importance of having access to pertinent training data, a topic we will address in the discussion.

8. Discussion and future work

Results obtained for the stylized examples and complex case studies suggest that probabilistic velocity model building is possible as long as training pairs in the form of velocity models and migrated image data are available. However, having access to representative training velocity models is challenging in practice. The examples presented here fall short because they are biased by our geological understanding, as expressed in synthetic earth models. To overcome these limitations and other challenges in applying the proposed methodology to more realistic settings, we strongly encourage our community to follow David Donoho's (Donoho, 2024) recipe for success in data science, which includes (i) making (training) datasets available; (ii) releasing research findings that can be reproduced in a frictionless manner; and (iii) establishing benchmarks to compare results based on quantitative figures of merit. We argue that this work contributes towards items (ii-iii). Item (i) remains challenging, but below we outline a possible strategy for addressing this item.

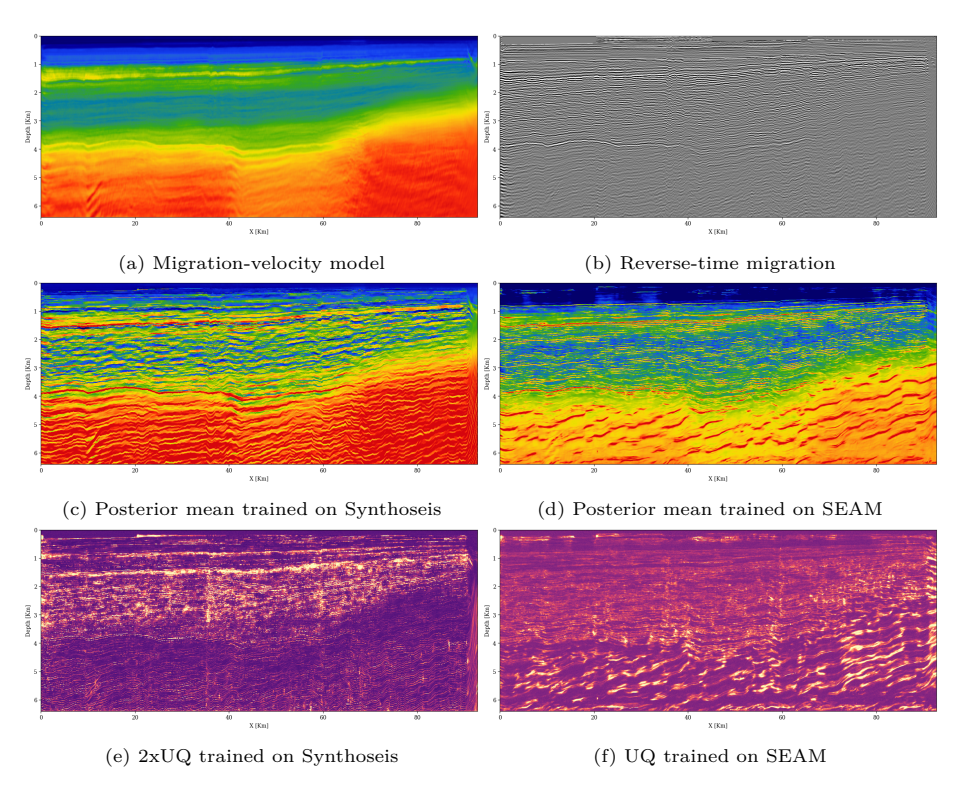


Figure 11: Field-data results trained on Synthoseis versus SEAM. (a) Migration velocity model used to produce RTM. (b) Observed RTM. (c) Mean of Posterior samples from Synthoseis. (d) Mean of Posterior samples from SEAM. We recommend zooming in a computer screen to see these figures.

A call to arms to curate datasets to train a foundation model. By using the latest tools from generative AI, Erdinc et al. (2024) recently developed a framework to train conditional neural networks to generate realistic Earth models parameterized by velocity. In their approach, Diffusion networks are trained on pairs imaged field data and well-log data, both residing in national data repositories such as the one maintained by the National Transition Authority in the United Kingdom. We are currently in the process of curating hundreds of 2D seismic image-well pairs, so that a foundational model can be trained with which realistic synthetic velocity can be generated without ever requiring access to velocity models themselves. As more curated datasets become available, the quality of this foundational model will improve, as will machine learning techniques that rely on training data.

An important avenue for future work is to explore non-amortized methods that would build on top of the amortized results shown here. Specifically, algorithms that use the forward operator at inference time to specialize to the observation and improve performance (Siahkoohi et al., 2023; Orozco et al., 2024; Yin et al., 2024a). This approach becomes especially pertinent when applying our method to field data.

9. Conclusions

We implemented machine learning enabled workflows that, through the use of modern conditional Diffusion neural networks, advance the state of the art in amortized migration-velocity model building with uncertainty quantification. In this context, amortization means that our network generalizes across different shot datasets. We also proposed a set of performance metrics as a benchmark to compare the effectiveness of different uncertainty quantification methods. For complex salt scenarios, we developed a new iterative workflow incorporating salt flooding. Using our Bayesian probabilistic approach, multiple migration-velocity models are generated from poor initial velocity models (e.g., models without salt). These samples from the posterior distribution produce different reversetime-migrated images that contain variability propagated from the uncertainty in the inferred velocity model. Thanks to machine learning, the proposed approach remains computationally feasible at inference time, with considerable but manageable offline training costs. The results represent a demonstration of machine learning enabled probabilistic velocity building from short-offset acoustic reflection-only data. While our evaluation on field datasets is still in its early stages, the initial results are promising. However, applying the method to field data revealed a bias toward the synthetic data distribution on which the networks were trained. This finding highlights the need to curate realistic training datasets to train the next generation of generative networks for solving geophysical inverse problems.

9.1. Acknowledgements

We are grateful to the Georgia Research Alliance and the ML4Seismic Center partners for their support in this work. We thank Devito Codes for providing a complimentary license and support of DevitoPro which greatly increased efficiency in producing the wave simulations. We thank Woodside Energy Group for providing access to the dataset referred to as "Galactic 2D", made available under Creative Commons BY-SA 4.0 licence [https://creativecommons.org/licenses/by-sa/4.0/] as part of Phase 2b of the 2023 Galactic 2D Seismic Imaging Study. We also thank Charles Jones (Osokey) for the valuable discussion.

References

- Alali, A., Kazei, V., Kalita, M., Alkhalifah, T., 2023. Deep learning unflooding for robust subsalt waveform inversion. Geophysical Prospecting 72, 7–19.
- Alemohammad, S., Casco-Rodriguez, J., Luzi, L., Humayun, A.I., Babaei, H., LeJeune, D., Siahkoohi, A., Baraniuk, R.G., 2023. Self-consuming generative models go mad. arXiv preprint arXiv:2307.01850.
- Alsing, J., Wandelt, B., 2018. Generalized massive optimal data compression. Monthly Notices of the Royal Astronomical Society: Letters 476, L60–L64.
- Baldassari, L., Siahkoohi, A., Garnier, J., Solna, K., de Hoop, M.V., 2024. Conditional score-based diffusion models for bayesian inference in infinite dimensions. Advances in Neural Information Processing Systems 36.
- Batzolis, G., Stanczuk, J., Schönlieb, C.B., Etmann, C., 2021. Conditional image generation with score-based diffusion models. arXiv preprint arXiv:2111.13606
- Bloem-Reddy, B., Whye, Y., et al., 2020. Probabilistic symmetries and invariant neural networks. Journal of Machine Learning Research 21, 1–61.
- Brunet, D., Vrscay, E.R., Wang, Z., 2011. On the mathematical properties of the structural similarity index. IEEE Transactions on Image Processing 21, 1488–1499.
- Cranmer, K., Brehmer, J., Louppe, G., 2020. The frontier of simulation-based inference. Proceedings of the National Academy of Sciences 117, 30055–30062.
- Donoho, D., 2024. Data science at the singularity. Harvard Data Science Review 6.
- Erdinc, H.T., Orozco, R., Herrmann, F.J., 2024. Generative geostatistical modeling from incomplete well and imaged seismic observations with diffusion models. arXiv preprint arXiv:2406.05136.
- Esser, E., Guasch, L., Herrmann, F.J., Warner, M., 2016. Constrained waveform inversion for automatic salt flooding. The Leading Edge 35, 235–239.
- Esser, E., Guasch, L., van Leeuwen, T., Aravkin, A.Y., Herrmann, F.J., 2018. Total variation regularization strategies in full-waveform inversion. SIAM Journal on Imaging Sciences 11, 376–406.

- Fehler, M., Keliher, P.J., 2011. Model development, in: SEAM Phase 1: Challenges of Subsalt Imaging in Tertiary Basins, with Emphasis on Deepwater Gulf of Mexico. Society of Exploration Geophysicists, pp. 15–50.
- Gahlot, A.P., Orozco, R., Yin, Z., Herrmann, F.J., 2024. An uncertainty-aware digital shadow for underground multimodal co2 storage monitoring. arXiv preprint arXiv:2410.01218.
- Gregor, K., LeCun, Y., 2010. Learning fast approximations of sparse coding, in: Proceedings of the 27th international conference on international conference on machine learning, pp. 399–406.
- Guo, C., Pleiss, G., Sun, Y., Weinberger, K.Q., 2017. On calibration of modern neural networks, in: International conference on machine learning, PMLR. pp. 1321–1330.
- Hennenfent, G., Herrmann, F.J., 2008. Simply denoise: Wavefield reconstruction via jittered undersampling. Geophysics 73, V19–V28.
- Ho, J., Jain, A., Abbeel, P., 2020. Denoising diffusion probabilistic models. Advances in neural information processing systems 33, 6840–6851.
- Hou, J., Symes, W.W., 2016. Accelerating extended least-squares migration with weighted conjugate gradient iteration. Geophysics 81, S165–S179.
- Izzatullah, M., Alali, A., Ravasi, M., Alkhalifah, T., 2024. Physics-reliable frugal local uncertainty analysis for full waveform inversion. Geophysical Prospecting .
- Jones, C., Edgar, J., Selvage, J., Crook, H., 2012. Building complex synthetic models to evaluate acquisition geometries and velocity inversion technologies, in: 74th EAGE Conference and Exhibition incorporating EUROPEC 2012, European Association of Geoscientists & Engineers. pp. cp–293.
- Jordan, M.I., Ghahramani, Z., Jaakkola, T.S., Saul, L.K., 1999. An introduction to variational methods for graphical models. Machine learning 37, 183–233.
- Karras, T., Aittala, M., Aila, T., Laine, S., 2022. Elucidating the design space of diffusion-based generative models. Advances in neural information processing systems 35, 26565–26577.
- Laves, M.H., Ihler, S., Fast, J.F., Kahrs, L.A., Ortmaier, T., 2020. Well-calibrated regression uncertainty in medical imaging with deep learning, in: Medical Imaging with Deep Learning, PMLR. pp. 393–412.
- Louboutin, M., 2024. slimgroup/imagegather.jl: v0.2.10 https://doi.org/10.5281/zenodo.12575836. Zenodo .

- Louboutin, M., Lange, M., Luporini, F., Kukreja, N., Witte, P.A., Herrmann, F.J., Velesko, P., Gorman, G.J., 2019. Devito (v3. 1.0): an embedded domain-specific language for finite differences and geophysical exploration. Geoscientific Model Development 12, 1165–1187.
- Louie, J.N., Pullammanappallil, S.K., Honjas, W., 2012. Advanced seismic imaging for geothermal development, in: SEG International Exposition and Annual Meeting, SEG. pp. SEG–2012.
- Luporini, F., Louboutin, M., Lange, M., Kukreja, N., Witte, P., Hückelheim, J., Yount, C., Kelly, P.H., Herrmann, F.J., Gorman, G.J., 2020. Architecture and performance of devito, a system for automated stencil computation. ACM Transactions on Mathematical Software (TOMS) 46, 1–28.
- Marino, J., Yue, Y., Mandt, S., 2018. Iterative amortized inference, in: International Conference on Machine Learning, PMLR. pp. 3403–3412.
- Merrifield, T.P., Griffith, D.P., Zamanian, S.A., Gesbert, S., Sen, S., De La Torre Guzman, J., Potter, R.D., Kuehl, H., 2022. Synthetic seismic data for training deep learning networks. Interpretation 10, SE31–SE39.
- Muller, A.P., Bom, C.R., Costa, J.C., Klatt, M., Faria, E.L., Silva, B.d.S., de Albuquerque, M.P., de Albuquerque, M.P., 2023. Deep-tomography: iterative velocity model building with deep learning. Geophysical Journal International 232, 975–989.
- Orozco, R., Siahkoohi, A., Louboutin, M., Herrmann, F.J., 2024. Aspire: Iterative amortized posterior inference for bayesian inverse problems. arXiv preprint arXiv:2405.05398.
- Orozco, R., Siahkoohi, A., Rizzuti, G., van Leeuwen, T., Herrmann, F.J., 2023. Adjoint operators enable fast and amortized machine learning based bayesian uncertainty quantification, in: Medical Imaging 2023: Image Processing, SPIE. pp. 365–375.
- Putzky, P., Welling, M., 2017. Recurrent inference machines for solving inverse problems. arXiv preprint arXiv:1706.04008.
- Qu, L., Araya-Polo, M., Demanet, L., 2024. Uncertainty quantification in seismic inversion through integrated importance sampling and ensemble methods. arXiv preprint arXiv:2409.06840 .
- Siahkoohi, A., Rizzuti, G., Orozco, R., Herrmann, F.J., 2023. Reliable amortized variational inference with physics-based latent distribution correction. Geophysics 88, R297–R322.
- Song, Y., Sohl-Dickstein, J., Kingma, D.P., Kumar, A., Ermon, S., Poole, B., 2020. Score-based generative modeling through stochastic differential equations. arXiv preprint arXiv:2011.13456.

- Sun, C., Malcolm, A., Kumar, R., Mao, W., 2024. Enabling uncertainty quantification in a standard full-waveform inversion method using normalizing flows. Geophysics 89, R493–R507.
- Sun, Y., Williamson, P., 2024. Invertible neural networks for uncertainty quantification in refraction tomography. The Leading Edge 43, 358–366.
- Tachella, J., Pereyra, M., 2023. Equivariant bootstrapping for uncertainty quantification in imaging inverse problems. arXiv preprint arXiv:2310.11838.
- Tarantola, A., 1984. Inversion of seismic reflection data in the acoustic approximation. Geophysics 49, 1259–1266.
- Wagner, F.M., Uhlemann, S., 2021. An overview of multimethod imaging approaches in environmental geophysics. Advances in Geophysics 62, 1–72.
- Witte, P., Yang, M., Herrmann, F., 2017. Sparsity-promoting least-squares migration with the linearized inverse scattering imaging condition: 79th conference and exhibition, eage, in: Expanded Abstracts.
- Wu, Z., Sun, Y., Chen, Y., Zhang, B., Yue, Y., Bouman, K.L., 2024. Principled probabilistic imaging using diffusion models as plug-and-play priors. arXiv preprint arXiv:2405.18782.
- Yang, L., Saad, O.M., Wu, G., Alkhalifah, T., 2024. Conditional image prior for uncertainty quantification in full waveform inversion. arXiv preprint arXiv:2408.09975.
- Yin, Z., Orozco, R., Herrmann, F.J., 2024a. Wiser: multimodal variational inference for full-waveform inversion without dimensionality reduction. arXiv preprint arXiv:2405.10327.
- Yin, Z., Orozco, R., Louboutin, M., Herrmann, F.J., 2024b. Wise: Full-waveform variational inference via subsurface extensions. Geophysics 89, A23–A28.
- Zhang, L., Sengupta, S., Parekh, C., Eliott-Lockhart, R., 2022. High-frequency fwi velocity model building for hydrocarbon delineation, in: SEG International Exposition and Annual Meeting, SEG. p. D011S043R004.
- Zhang, X., Lomas, A., Zhou, M., Zheng, Y., Curtis, A., 2023. 3-d bayesian variational full waveform inversion. Geophysical Journal International 234, 546–561.
- Zhao, X., Curtis, A., 2024. Variational prior replacement in bayesian inference and inversion. Geophysical Journal International 239, 1236–1256.
- Zhao, X., Curtis, A., Zhang, X., 2022. Bayesian seismic tomography using normalizing flows. Geophysical Journal International 228, 213–239.
- Zheng, K., Lu, C., Chen, J., Zhu, J., 2023. Improved techniques for maximum likelihood estimation for diffusion odes, in: International Conference on Machine Learning, PMLR. pp. 42363–42389.